Section 6

Developments in global forecast models,
case studies, predictability investigations,
global ensembles.

Modeling of Chemical Tracer Transport in the Atmospheric Environment and its Impact on the Global Climate

Z. N. Begum

Ex-Scientist "G'/Advisor, Department of Science and Technology, New Delhi, India
and
OWSD Full Member, ICTP Campus, Trieste, Italy

Continental regions are experiencing rapid environmental changes due to expansion of industrial activities and land uses in different types of agricultural productions, burning of fossil fuels etc., which lead to the emanation of huge amount of smog aerosol particulates and chemicals in the atmosphere. Information about these chemical tracers has been found from Indian Ocean Experiment (INDOEX) as well as through Intergovernmental Panel for Climate Change (IPCC) assessment reports and from some other sources. In this paper, we have used a global atmospheric model in which the optical properties and the concentrations of the chemical tracers and aerosols have been incorporated. The aerosols and chemicals are transported in the atmospheric environment by the model cumulus convection and through the model semi-Lagrangian advection process. Thus, they are globally distributed along with the wind flow. The model has been used in studying the impact of the tropospheric chemical perturbations on the global environment.

The perturbation in atmospheric trace gases (viz. SO_2 , O_3 , CO, CO_2 , H_2O, CH_4 , NO_2 and CFC etc.) is an important factor in climate change. During INDOEX and IPCC, both satellite and ground based campaigns have been carried out to study the role of aerosols (continental and marine) and trace gas species in the radiative forcing of the atmosphere. The presence of greenhouse gases in the atmosphere and their increasing or decreasing concentrations change the equilibrium point and affect our environment. Atmospheric aerosols and gases are either injected directly into the atmosphere or produced by gas to particle conversion. Emissions of anthropogenic aerosols and gases to the troposphere have increased in recent decades, and the consequent increase in their concentrations may effect the global climate. Modeling the aerosol effects include scattering and absorption of incident solar radiation (direct effect) and modifying the microphysical and optical properties of clouds (indirect effect). Changing optical properties, the chemical tracers modify the radiation field in the atmosphere and determine the scattering losses and absorption of radiative energy and consequently influence the climate and the environment. The model used in this work is based on the NMC (USA) model of Kanamitsu (1989) and Begum (2003, 2020). The tracer transport along with the wind flow are explicitly resolved by the model following the semi-Lagrangian advection scheme.

The results are displayed in Fig. 1 in which we have plotted the change of the temperatures derived from the present model for the years 1996 to 1999 and validated the same with those reported by other workers (Houghton et al., 2001 and Hansen et al., 2000, 2001, 2002). It is found that the model derived values, though slightly differ from the observed values, show similar trend for the temperature change, increasing gradually year after year. The observed global warming trend is therefore thought to be caused by a shifting of the equilibrium conditions of the past, as a result of the build-up of certain gases and perturbations in the atmosphere,

especially due to the increase of greenhouse gases. This results in the absorption of the IR radiation by the atmosphere, producing a warming influence in the surface air temperature.
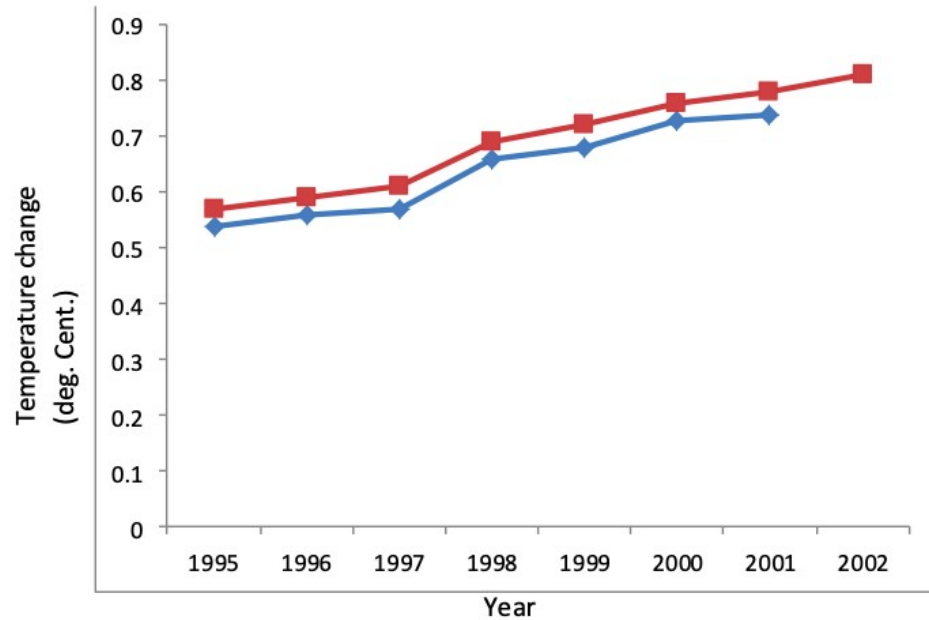

Fig. 1: Plots of Temperature Change versus Year as computed from the Global Circular Model based on: ◆ Kanamitsu. M. (1989) [Original Model]; ■ Begum, Z.N. (2003).

REFERENCES

Begum, Z.N.: 2003, 'A theoretical investigation of the radiative effects and microphysical processes involved in the interaction of aerosol particulates in the atmosphere and validation of the theoretical results with the INDOEX observations', J. Quant. Spect. Rad. Trans. **78**, 99-103.

Begum, Z.N.: (2020), Investigations of the International Experiments, GAME and I-STEP and the Global Atmospheric Model Findings; Res. Activ. Earth System Modell. E.Astakhova (ed.). Rep. No 50. WCRP Rep. No. 6/2020: p. 6-05.

Houghton, J.T, Y. Ding, D.J. Griggs, M. Noguer, P.J. van der Linden and D Xiaosu (eds); Climate Change 2001: The Scientific Basis. Contribution of Working Group I to the Third Assessment Report of the Intergovernmental Panel on Climate Change (IPCC). New York, Cambridge University Press.

Kanamitsu, M.:1989, 'Description of the NMC global Data Assimilation and Forecast System', Weather and Forecasting, **4** , 335-342.

Associated with Pacific Decadal Oscillation regional natural hazards like Amur River record flood in 2013 and oceanic red tide near Kamchatka Peninsula in 2020

Mokhov I.I.
[1]A.M. Obukhov Institute of Atmospheric Physics RAS
[2]Lomonosov Moscow State University
mokhov@ifaran.ru

In the fall 2020 an extraordinary ecological situation with mass death of hydrobionts and unnatural color and odor of oceanic water near Kamchatka Peninsula was noted. It was associated with strong positive anomalies of sea surface temperature (SST) in this region in summer-fall months which facilitated to formation of so called red tide with harmful bloom of algae, responsible for death of hydrobionts in coastal zones near Kamchatka Peninsula [1].
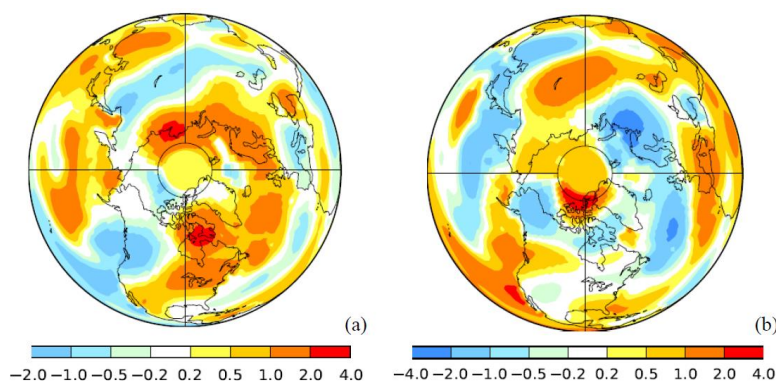

Fig. 1. Surface temperature differences [K] between 2020 and 2015 (a) and between 2015 and 2013 in summer by GISS data.

Several factors contribute to the increased risk of the formation of such regional climatic and ecological anomalies, in particular in the Pacific coastal zones. In [2,3], among the reasons for the formation of a record flood in the Amur River basin in 2013, it was noted against the background of a long-term significant tendency of global and regional warming the atmospheric blocking over the Pacific Ocean during the monsoon season (August-September) in the negative phase of the Pacific Decadal Oscillation (PDO) with positive surface temperature anomalies in the western part of the Pacific Ocean off the Asian coasts (the role of El Nino phases and West Pacific teleconnection pattern was also noted).
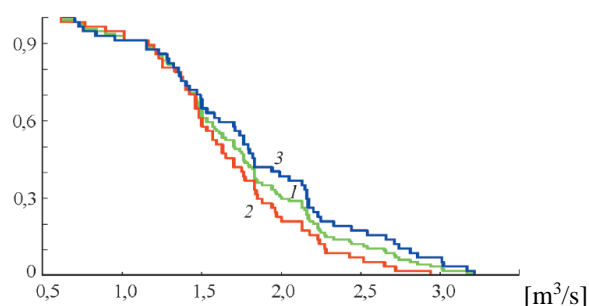

Fig. 2. Probability of exceeding the Amur River runoff [m3/s] in August of various levels from observations for the period 1900-2013 (1, green curve) and separately for the positive (2, red curve) and negative (3, blue curve) PDO phases.

The significance of regional temperature anomalies in different PDO phases is illustrated in Fig. 1, representing the temperature differences between years in the negative PDO phase (2013 and 2020) and in the positive PDO phase (2015). (In the positive phase of PDO, in particular in 2015, surface temperature anomalies in the western Pacific are negative.) Against the background of general warming, with significant positive SST anomalies in the west part of the Pacific Ocean

associated with a negative PDO phase, as in 2020 (see Fig. 1), increases the risk of formation of red tides in the coastal zones of the Far East. Connection with PDO of red tides was noted in other regions, in particular, in the coastal zones of North America [4-6].

The data obtained in [2,3] indicate the potential for the influence of PDO on the formation of the extreme runoff of the Amur River during the period of monsoon activity. In particular, 8 out of 10 years with the highest discharge of the Amur River in August since 1900 corresponded to the negative PDO phase. Figure 2 shows the probability of exceeding the Amur River runoff [m³/s] in August of various levels from observations since 1900 and separately for the positive and negative PDO phases.
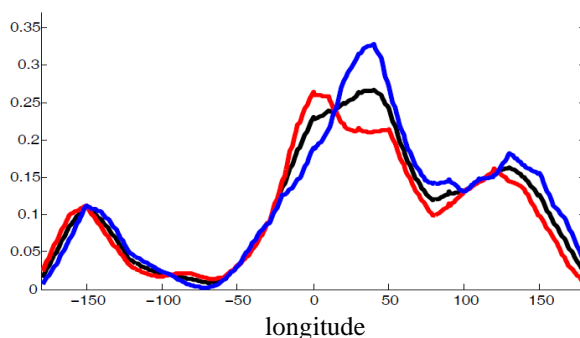

Fig. 3. Frequency of atmospheric blockings in dependence on longitude in the Northern Hemisphere in summer for the period 1969-2013 (black curve) and separately for negative (blue curve) and positive (red curve) PDO phases.

Significant role in the formation of climatic extremes like Amur River flood in 2013 is associated with atmospheric blockings. Figure 3 shows that the frequency of atmospheric blockings over west part of Pacific Ocean in the Northern Hemisphere in summer for the period 1969-2013 is highest in the negative PDO phase [3]. According to [7], atmospheric blockings, particularly in July-August-September, in the Northern Hemisphere as a whole by data for last decades are more frequent and intense in negative PDO phase.

References

[1] Bondur V.G., Zamshin V.V., Chvertkova O. I. Space study of a red tide-related environmental disaster near Kamchatka Peninsula in September–October 2020. *Doklady Earth Sci.* 2021 **497** (1): 255–260.
[2] Mokhov I.I. (2014) Hydrological anomalies and tendencies of change in the basin of Amur River under global warming. *Doklady Earth. Sci.*, **455** (2): 459-462.
[3] Mokhov I.I., Khon V.Ch., Timazhev A.V., Chernokulsky A.V., Semenov V.A. (2014) Hydrological anomalies and trends in the Amur river basin due to climatic changes. *In: Extreme Floods in the Amur River Basin: Causes, Forecasts and Recommendations*, Moscow, Roshydromet, 81-120. (in Russian)
[4] Hooff RC, Peterson WT (2006) Copepod biodiversity as an indicator of changes inocean and climate conditions of the northern California current ecosystem. *Limnol. Oceanogr.* **51** (6): 2607–2620.
[5] McKibben S.M., Peterson W., Wood A.M., Trainer V.L., Hunter M., White A.E. (2017) Climatic regulation of the neurotoxin domoic acid. *Proc. N.A.S.*, **114** (2): 239–244.
[6] Corters-Altamirano R., Alonso-Rodrırguez R., Salas-de-Leorn D.A. (2019) Historical observations of algal blooms in Mazatlan Bay, Sinaloa, Mexico (1979-2014). *PLoS ONE,* **14** (1): e0210631. https://doi.org/10.1371/journal.pone.0210631
[7] Lupo A.R., Jensen A.D., Mokhov I.I., Timazhev A., Eichler T., Efe B. (2019) Changes in global blocking character during recent decades*. Atmosphere.* **10** (2): 92. https://doi.org/10.3390/atmos10020092

Predictability of seasonal temperature anomalies in the North Eurasian regions in the La Niña conditions

Mokhov I.I.[1,2]
[1]A.M. Obukhov Institute of Atmospheric Physics RAS
[2]Lomonosov Moscow State University
mokhov@ifaran.ru

The impact of the El Niño / La Niña events is significant on a global scale, including North Eurasian regions [1-5]. In [3] estimates of possible anomalies in Russian regions in spring-summer months were obtained, taking into account the La Niña phase and the forecasts of its transformation by the end of the year. Similar estimations are presented here for 2021 with the beginning in the La Niña phase with negative anomalies of sea surface temperature in the central and eastern equatorial regions of the Pacific Ocean. According to CPC/IRI official probabilistic ENSO forecast at the beginning of May on the basis of ensemble model simulations the probability of the L-phase continuation to the end of 2021 ($L{\rightarrow}L$ transition) is expected about 50%. The corresponding probability for N-phase ($L{\rightarrow}N$ transition) is expected less than 40% and about 10% for E-phase ($L{\rightarrow}E$ transition).

Here, the May-June-July anomalies of surface air temperature (SAT) δT and precipitation δP for European (ER) and Asian (AR) Russian regions in mid-latitudes based on observations since 1891 [6] are analyzed. For estimation of the El Niño / La Niña effects, we used their indices characterized by the sea surface temperature in the Niño3, Nino3,4 and Nino4 regions in the equatorial latitudes of the Pacific Ocean. The El Niño (E), La Niña (L) and neutral (N) phases are defined similar to [1].

Table 1. Probability of positive and negative surface air temperature anomalies (δT) in the ER (and AR) in May-June-July for different transitions from La-Nina conditions at the beginning of the year (characterized by indices Nino3, Nino3,4 and Nino4) from observations since 1891.

δT, K		Nino3 $n=29$			Nino3.4 $n=36$			Nino4 $n=28$		
		$L{\rightarrow}E$ $n=7$	$L{\rightarrow}L$ $n=9$	$L{\rightarrow}N$ $n=13$	$L{\rightarrow}E$ $n=11$	$L{\rightarrow}L$ $n=14$	$L{\rightarrow}N$ $n=11$	$L{\rightarrow}E$ $n=4$	$L{\rightarrow}L$ $n=10$	$L{\rightarrow}N$ $n=14$
>0	>0		0.41 (0.62)			0.50 (0.56)			0.43 (0.54)	
		0.57 (0.71)	0.33 (0.56)	0.38 (0.62)	0.55 (0.64)	0.36 (0.64)	0.64 (0.36)	0.50 (0.50)	0.40 (0.50)	0.43 (0.57)
	>1K		0.17 (0.21)			0.25 (0.25)			0.21 (0.25)	
		0.29 (0.14)	0.11 (0.22)	0.15 (0.23)	0.27 (0.18)	0.21 (0.21)	0.27 (0.36)	0.25 (0.25)	0.20 (0.20)	0.21 (0.29)
≤0	≤0		0.59 (0.38)			0.50 (0.44)			0.57 (0.46)	
		0.43 (0.29)	0.67 (0.44)	0.62 (0.38)	0.45 (0.36)	0.64 (0.43)	0.36 (0.64)	0.50 (0.50)	0.60 (0.50)	0.57 (0.43)
	≤-1K		0.14 (0.10)			0.08 (0.11)			0.07 (0.07)	
		0.29 (0.29)	0 (0)	0.15 (0.08)	0.18 (0.18)	0.07 (0)	0 (0.18)	0 (0.25)	0.10 (0)	0.07 (0.07)

Table 1 shows the estimates for probability of the May-June-July temperature anomalies δT in the ER (and AR) for different transitions from the L-phase at the beginning of the year with

the use of different El Niño indices. According to these May-June-July estimates in general there are more probable positive temperature anomalies in the AR and negative temperature anomalies in the ER.

Table 2. Probability of positive and negative precipitation anomalies (δP) in the ER (and AR) in May-June-July for different transitions from La-Nina conditions at the beginning of the year.

δP [%]		Nino3 n=29			Nino3.4 n=36			Nino4 n=28		
		L→E n=7	L→L n=9	L→N n=13	L→E n=11	L→L n=14	L→N n=11	L→E n=4	L→L n=10	L→N n=14
<0	<0		0.41 (0.45)			0.56 (0.36)			0.50 (0.46)	
		0.43 (0.57)	0.56 (0.56)	0.31 (0.31)	0.64 (0.45)	0.43 (0.36)	0.64 (0.27)	0.50 (0.75)	0.60 (0.50)	0.43 (0.36)
	<-20%		0.10 (0.14)			0.11 (0.11)			0.11 (0.14)	
		0.14 (0.29)	0.22 (0.11)	0 (0.08)	0.09 (0.18)	0.14 (0.07)	0.09 (0.09)	0 (0.25)	0.20 (0.10)	0.07 (0.14)
≥0	≥0		0.59 (0.55)			0.44 (0.64)			0.50 (0.54)	
		0.57 (0.43)	0.44 (0.44)	0.69 (0.69)	0.36 (0.55)	0.57 (0.64)	0.36 (0.73)	0.50 (0.25)	0.40 (0.50)	0.57 (0.64)
	>20%		0.03 (0.10)			0.03 (0.08)			0.04 (0.04)	
		0 (0.14)	0 (0)	0.08 (0.15)	0 (0.09)	0 (0)	0.09 (0.18)	0 (0)	0 (0)	0.07 (0.07)

Table 2 shows corresponding estimates for probability of positive and negative precipitation anomalies (δP) in the ER (and AR) in May-June-July for different transitions from La-Nina conditions at the beginning of the year.

References
[1] Mokhov I.I., Timazhev A.V. (2015) Drought risk in the North Eurasian regions: Assessment of El-Nino effects. *Res. Activ. Atmos. Ocean. Modell.* E. Astakhova (ed.). WCRP Rep. No.12/2015, 2015, 2.6–2.7.
[2] Mokhov I.I., Timazhev A.V. (2016) Weather-climate anomalies in Russian regions: El Niño-associated predictability. *Res. Activ. Atmos. Ocean. Modell*. E. Astakhova (ed.). WCRP Rep. No.15/2016: 6.09–6.10.
[3] Mokhov I.I., Timazhev A.V. (2018) Predictability of weather-climate anomalies in the North Eurasian regions during transitions from the La Nina conditions. *Res. Activ. Atmos. Ocean. Modell.* E. Astakhova (ed.). Rep. No 48. WCRP Rep. No 15/2018: 6.09-6.10.
[4] Mokhov I.I., Timazhev A.V. (2019) Predictability of weather-climate anomalies in the North Eurasian regions for different ENSO transitions during last decades. *Res. Activ. Atmos. Ocean. Modell.* E. Astakhova (ed.). Rep. No 49. WCRP Rep. No. 12/2019: 6.09-6.10.
[5] Mokhov I.I., Timazhev A.V.(2020) Climate anomalies in the North Eurasian regions: predictability for different El-Nino conditions. *Res. Activ. Earth System Modell*. E. Astakhova (ed.). Rep. No 50. WCRP Rep. No. 6/2020: 6.09-6.10.
[6] Meshcherskaya A.V., Mirvis V.M., Golod M.P. (2011) The drought in 2010 against the background of multiannual changes in aridity in the major grain-producing regions of the European part of Russia. *Tr. MGO* **563**: 94–121 (in Russian)

Upgrade of JMA's Operational Global NWP system

UJIIE Masashi, HIGUCHI Mayuko, KADOWAKI Takashi, KUROKI Yukihiro, MIYAOKA Kengo, ODA Mayuko, OCHI Kenta, SEKIGUCHI Ryohei, SHIMIZU Hiroyuki, YOKOTA Sho, and YONEHARA Hitoshi

Japan Meteorological Agency, Tokyo, Japan

(email: ujiie@met.kishou.go.jp)

1. Introduction

The Japan Meteorological Agency (JMA) upgraded its operational global Numerical Weather Prediction (NWP) system (JMA 2019) in March 2021 to incorporate the enhanced vertical resolution of the JMA Global Spectral Model (GSM), improved land surface analysis and an upgraded atmospheric data assimilation system (Kadowaki et al. 2020). These improvements resulted in better forecasting (Yonehara et al. 2020), particularly for the Northern Hemisphere. This report outlines individual components of the upgrade and related verification results.

2. Major Updates

2.1 Number of Vertical Levels

The number of vertical levels of the GSM was increased from 100 to 128, with the uppermost level maintained at 0.01 hPa. Vertical grid spacing is now 1.2 – 1.3 times finer over the troposphere and stratosphere than before. The enhanced vertical resolution reduces discretization errors in the dynamical process and improves atmospheric representation.

2.2 Snow Depth Analysis

In the upgraded system, forecast snow depth corrected using satellite-estimated snow area data is employed as the first guess for snow depth analysis, as opposed to the climatological values employed with the previous system. Harnessing with the upgrade of the first guess, correlation length and magnitude of background error are optimized to increase the contribution of the first guess to analysis. These improvements mitigate excessive spread of snow analysis data over observation-sparse areas, and reduce systematic errors in shortwave radiative fluxes for snow-covered surfaces.

2.3 Soil Moisture Analysis

The upgraded system employs soil moisture analysis based on Ochi (2020) assimilating screen-level temperature and relative humidity analysis using a simplified Extended Kalman Filter. The system initializes soil moisture from the surface to a depth of 0.19 m, as opposed to the previous system's employment of climatological values.

This upgrade enables representation of soil moisture variations associated with daily weather conditions and reduces temperature errors for the lower troposphere.

2.4 Atmospheric Data Assimilation System

To optimize estimation of flow-dependent background error covariance (referred to here as **B**) in the four-dimensional variational data assimilation system, the number of ensemble members used to create ensemble-based **B** has been increased from 50 to 100, and the related weight has also been increased (Yokota et al. 2021). Climatological **B** has also been updated based on error statistics for the latest GSM.

These improvements result in better fitting of the first guess to observation data such as those

from radiosondes and satellite radiances in the atmospheric data assimilation system.

3. Verification Results

Twin experiments conducted to evaluate the performance of the updated (TEST) system against the previous (CNTL) system for July to September 2019 (summer) and December to February 2019/2020 (winter) showed that the land surface analysis upgrade reduced systematic errors in the lower atmosphere. As an example, Figure 1 shows vertical profiles of mean errors (MEs) in temperature for CNTL and TEST averaged from September 2019 to February 2020. The upgraded system reduced cold biases in the lower troposphere, partially due to suppression of excessive spread in snow data. As a synthetic effect of these major forecast upgrades, TEST showed significantly reduced root-mean-square errors (RMSEs) for 500-hPa geopotential height over forecasts of several days (Figure 2).

References

Kadowaki, T., Y. Ota, and S. Yokota, 2020: Introduction of a new hybrid data assimilation system for the JMA Global Spectral Model. WGNE. Res. Activ. Earth. Sys. Modell., 50, 1.9-1.10.

Japan Meteorological Agency, 2019: Outline of Operational Numerical Weather Prediction at JMA. Japan Meteorological Agency, Tokyo, Japan.

Ochi, K., 2020: I Preliminary results of soil moisture data assimilation into JMA Global Analysis. WGNE. Res. Activ. Earth. Sys. Modell., 50, 1.15-1.16.

Yokota S., T. Kadowaki, M. Oda and Y. Ota, 2021: Improving ensemble-based background error covariances of the hybrid 4DVar in JMA global analysis. WGNE. Res. Activ. Earth. Sys. Modell, submitted.

Yonehara, H., C. Matsukawa, T. Nabetani, T. Kanehama, T. Tokuhiro, K. Yamada, R. Nagasawa,Y. Adachi, and R. Sekiguchi, 2020: Upgrade of JMA's Operational Global Model.

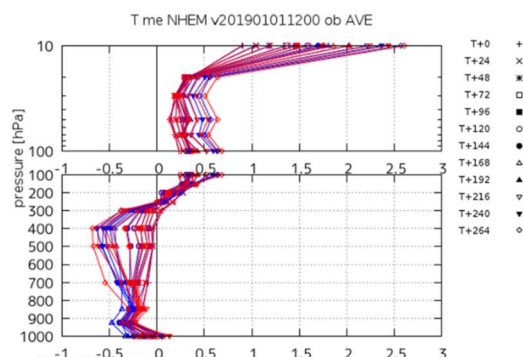WGNE. Res. Activ. Earth. Sys. Modell, 50, 6.19-6.20.

Figure 1. Vertical profiles of mean errors for temperature [K] in the 0 – 180°E, 20 – 90°N region for the winter experiment. Blue: CNTL; red: TEST. Lines represent ME at different forecast lead times for days 1 to 11.
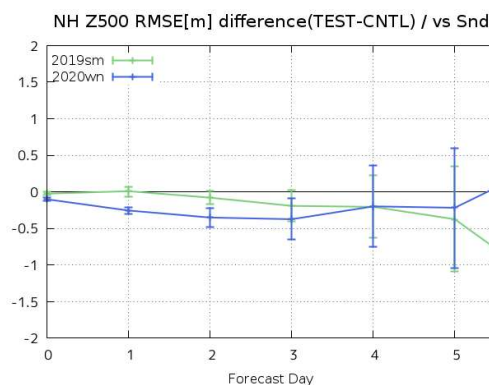

Figure 2. Root-mean-square error differences (TEST – CNTL) of 500-hPa geopotential height [m] against radiosonde (Snd) in the Northern Hemisphere extra-tropics (20 – 90°N) in the summer and winter experiments. The horizontal axis shows the forecast lead time [days], and the green and blue lines show the summer and winter experiments, respectively. Error bars indicate statistical significance with 95% confidence based on the bootstrap method.

Impact of Aircraft High-Density Observations on GFSv16 Tropical Cyclone Forecasts

Xingren Wu[1], Daryl Kleist[2], Vijay Tallapragada[2], Fanglin Yang[2], and Jason A. Sippel[3]

[1]IMSG at EMC/NCEP/NWS/NOAA, College Park, MD 20740, [2]EMC/NCEP/NWS/NOAA, College Park, MD 20740, [3]NOAA/AOML/Hurricane Research Division, Miami, FL 33149

Email: Xingren Wu@noaa.gov

1.   Introduction

High-density observation (HDOB) data are assimilated in the operational Hurricane Weather Research and Forecast (HWRF) model. HDOBs include flight-level wind, temperature, and moisture measurements, and SFMR-derived surface wind speeds from the NOAA P-3, NOAA G-IV and Air Force Reserve Command C-130 aircraft. The assimilation of HDOB data in HWRF showed a considerable benefit (Tong *et al*. 2018) for tropical cyclone forecasts. HWRF has also implemented many enhancements to the aircraft data assimilation, including utilization of inner core dropsondes and drift corrections for dropsondes. Changes to the NCEP Global Forecast System (GFS) have been driven by the successes in HWRF data assimilation. There is also a need for the improved use of aircraft reconnaissance data (such as HDOBs and dropsondes), with specific requests from the Air Force, Air Operations Center, and National Hurricane Center to add HDOB data into GFS.

2.   Model and Experiments

In this study the NCEP pre-operational GFS version 16 (GFSv16) was used to examine the impact of HDOB data on the GFS forecast for hurricanes. GFSv16 is based on GFS version 15 (GFSV15), which was developed with the finite volume cubed-sphere dynamical core and microphysics from GFDL. Changes in GFSv16 include increasing the vertical resolution from 64 to 127 levels and moving the model top to 80 km height, improved physics, using a Local Ensemble Kalman Filter with model space localization and linearized observation operator, and employing the 4-Dimensional Incremental Analysis Update technique (4D-IAU) for data assimilation (DA). The experiments to assimilate HDOB data were set up and run using the same GFSv16 pre-operational version for reforecast with a 6-hourly DA cycle, over the following selected periods with available HDOB data: (1) 20180902-20180919, (2) 20190822-20191002, (3) 20200601-20200612, and (4) 20200721-20200806.

3.   Track and Intensity Analysis

Track and intensity are analyzed from the HDOB experiment (V16H), and compared to the GFSv16 reforecast (V16R) and GFSv15 operational forecast (GFSO) or reforecast (prior to GFSv15's implementation into operations). Figure 1 shows the model forecast track error and skill over the Atlantic for strong storms (with the maximum wind greater than 50 kts). Improvements are clearly observed in V16H, with less track error and an increase in track forecast skill (8-16% for day 1 to day 6). The improvements in the intensity forecast were also clear for forecast lead times greater than 48 hours (Figure 2). When all the hurricanes cases were considered, the improvements in track skill are 3-8% and the intensity forecast is neutral (not shown). For the West Pacific, similar improvements were also observed. However, for the Eastern Pacific basin, the impact is neutral on the track forecast and there is slight degradation in the intensity (not shown). Based on these positive impacts, the HDOB was added to GFSv16 for operations.
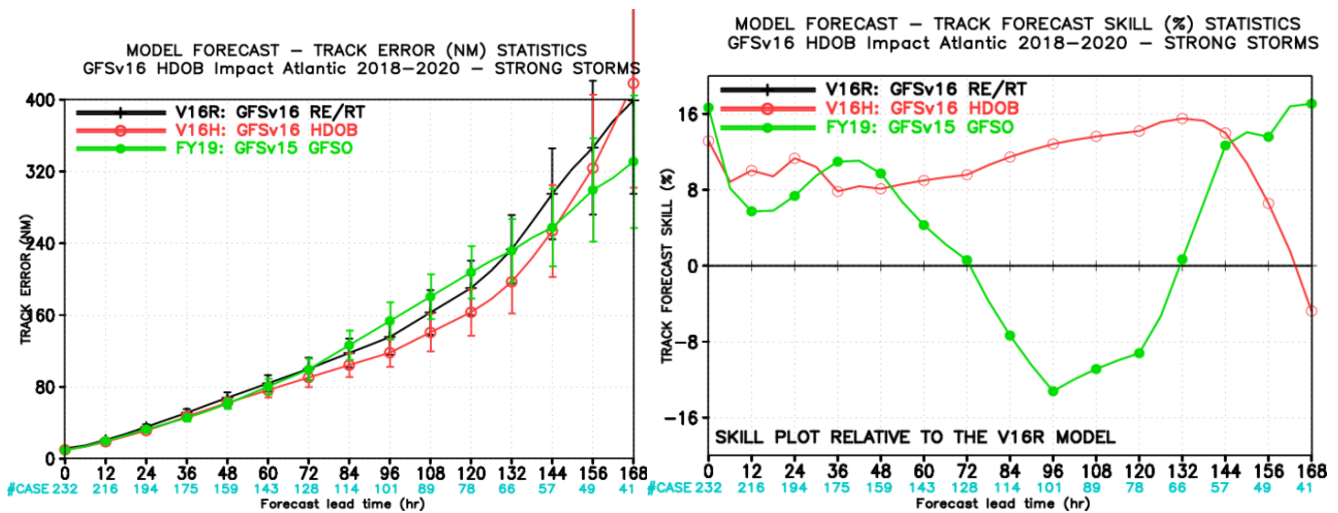
Figure 1. Model forecast track error (left) and skill (right) from GFSv16 reforecast (V16R, black), HDOB experiment (V16H, red) and GFSv15 (GFSO, green) from 2018-2020 for Atlantic strong storms (maximum wind greater than 50 kts).
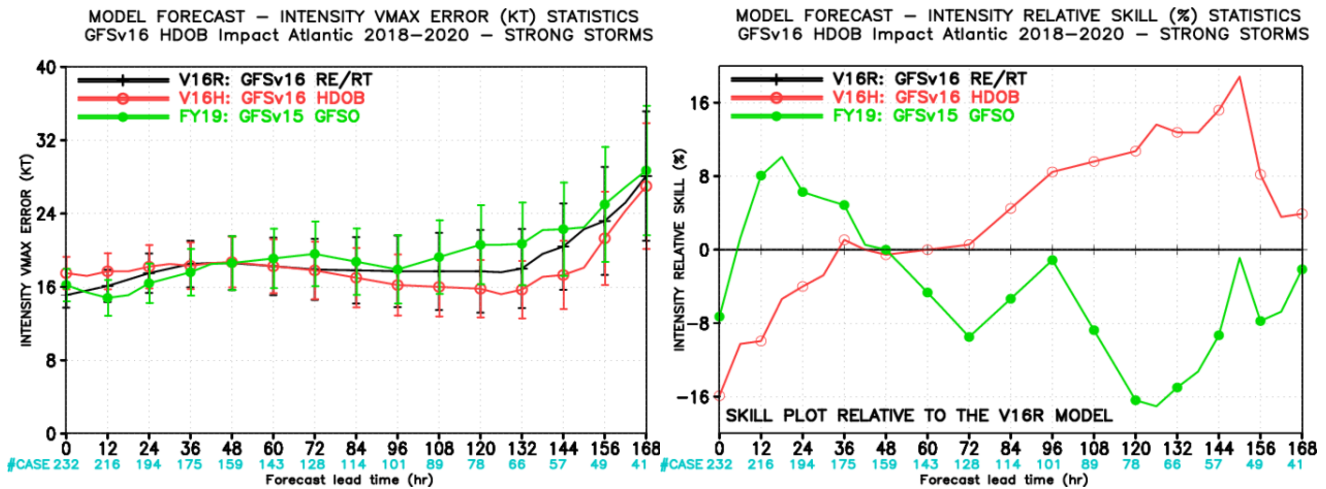

Figure 2. Model forecast intensity error (left) and relative skill (right) from GFSv16 reforecast (V16R, black), HDOB experiment (V16H, red) and GFSv15 (GFSO, green) from 2018-2020 for Atlantic strong storms (maximum wind greater than 50 kts).

References

Tong, M., and co-authors, 2018: Impact of Assimilating Aircraft Reconnaissance Observations on Tropical Cyclone Initialization and Prediction Using Operational HWRF and GSI Ensemble–Variational Hybrid Data Assimilation. *Mon. Wea. Rev., 146,* 4155-4177, https://doi.org/10.1175/MWR-D-17-0380.1.

Upgrade of JMA's Global Ensemble Prediction System

YAMAGUCHI Haruki, IKEGAMI Masaaki, IWAHIRA Tomoya, OCHI Kenta,
SEKIGUCHI Ryohei, and TAKAKURA Toshinari

Japan Meteorological Agency
e-mail: h.yamaguchi@met.kishou.go.jp

1. Introduction

The Japan Meteorological Agency (JMA) upgraded its Global Ensemble Prediction System (Global EPS) on March 30 2021 to incorporate recent Global Spectral Model (GSM) developments, an increased ensemble size and improved initial perturbations.

2. Major Updates

    (1) Incorporation of Recent GSM Developments

    The forecast model was upgraded to a low-resolution version of the newly revised Global Spectral Model (GSM; Ujiie et al. 2021) with enhanced vertical resolution based on an increased number of model levels (100 to 128) with the top level maintained at 0.01 hPa.

    (2) Increased Ensemble Size

    The ensemble size was increased (Table 1) for forecasts with lead times up to 264 hours from 27 to 51. For others from 264 to 432 hours, and the ensemble size was increased from 13 to 51, and operation frequency was reduced to once a day (12 UTC) from twice a day (00 and 12 UTC), thereby almost doubling the daily total ensemble size. For forecasts at lead times from 432 to 816 hours, operation at the 00 UTC initial time was also terminated and the ensemble size was enhanced from 13 to 25.

    (3) Improved Initial Perturbations

    Singular vector (SV)-based initial perturbations were improved by implementing up to 50 modes as opposed to the 25 modes of the old system for each target area of the Northern Hemisphere ($30 - 90°N$) and the Southern Hemisphere ($90 - 30°S$). In combination with the adjusted amplitudes for initial perturbations, this change reduced overestimation of ensemble spread for 500-hPa geopotential height forecasts in mid-latitudes at lead times of around 24 to 72 hours as well as ensemble mean forecast errors. The total SV energy norm was also modified to terminate contribution from above 50 hPa to avoid SV computation with a large peak of energy in the upper stratosphere.

3. Verification Results

To verify system performance for medium-range forecasts with lead times of up to 11 days, retrospective forecast experiments covering periods of three months or more in summer 2019 and winter 2019/20 were conducted. The results showed improved CRPS performance for several elements, including 850 hPa temperature, 500 hPa geopotential height and 250 hPa winds, in mid-latitudes for both seasons. Figure 1 shows CRPSs for 500 hPa geopotential height in winter. Brier skill scores for precipitation forecasts in Japan were also improved (not shown).

To examine the effects of increased ensemble size up to 18 days, hindcast experiments for the period from 2014 to 2018 were also conducted using the Japanese 55-year Reanalysis (JRA-55; Kobayashi et al. 2015) dataset for atmospheric initial conditions. The ensemble sizes per initial day were 26 (CNTL) and 51 (TEST), and the same forecast model was used. The results showed that forecast skill for several elements such as temperature at 850 hPa, geopotential height at 500 hPa and mean sea level pressure were improved for all seasons. Figure 2 highlights improved Brier skill scores for geopotential height at 500 hPa in the Northern Hemisphere ($20 - 90°N$).

References

Kobayashi, S., Y. Ota, Y. Harada, A. Ebita, M. Moriya, H. Onoda, K. Onogi, H. Kamahori, C. Kobayashi, H. Endo, K. Miyaoka, and K. Takahashi, 2015: The JRA-55 reanalysis: General specifications and basic characteristics. J. Meteor. Soc. Japan., 93, 5-48.

Ujiie, M., M. Higuchi, T. Kadowaki, Y. Kuroki, K. Miyaoka, M. Oda, K. Ochi, R. Sekiguchi, H. Shimizu, S. Yokota, and H. Yonehara, 2021: Upgrade of JMA's Operational Global NWP system. *Res. Activ. Earth Sys. Modell.*, WGNE Rep.No. 51. WCRP Rep. No.4/2021. July 2021, WMO, Geneva. pp. 6-09-6-10.

Table 1: Ensemble sizes and initial times for the old and new Global EPS. NUM represents ensemble size per initial time, and INI represents initial times (UTC).

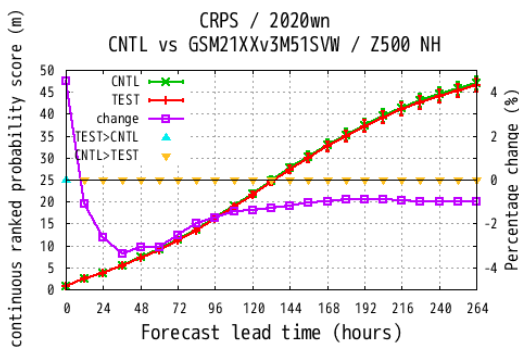| Lead time		Old	New
Initial time – 132 hours	NUM	27	51
	INI	06, 18	06, 18
Initial time – 264 hours	NUM	27	51
	INI	00, 12	00, 12
264 – 432 hours	NUM	13	51
	INI	00, 12	12
432 – 816 hours (Tuesday and Wednesday runs only)	NUM	13 11 for Tuesdays at 00 UTC	25
	INI	00, 12	12

Figure 1: CRPSs of 500 hPa geopotential height forecasts against analysis for the Northern Hemisphere (20 − 90°N) during winter 2019/20 as a function of forecast lead times up to 264 hours. The red and green lines represent verification results for the new (TEST) and previous (CNTL) Global EPS (left axis; unit: m), and the purple line represents ratios of change in scores ([TEST −CNTL]/CNTL, right axis; unit: %). Error bars indicate two-sided 95% confidence levels, and triangles (TEST < CNTL or CNTL > TEST) indicate a statistically significant difference of 0.05.
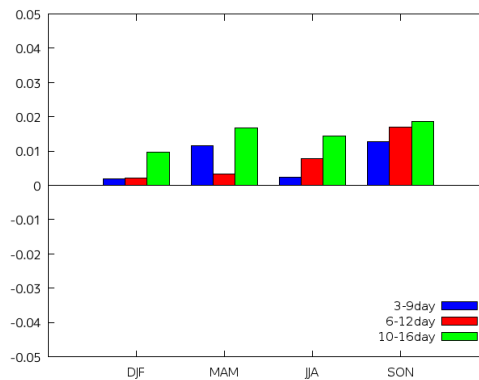

Figure 2: Brier skill score (BSS) differences for geopotential height at 500 hPa in the Northern Hemisphere (20 − 90°N) for each season. Positive values represent BSSs of the new Global EPS exceeding those of the previous Global EPS. BSSs are for the above-, near- and below-normal probability categories.

The Global Forecast System Model Instability Issue and Potential Solutions

Xiaqiong Zhou[1] and Hann-Ming Henry Juang[2]
[1]CPAESS UCAR at GFDL/NOAA, Princeton, NJ   [2]EMC NCEP/NOAA, College Park, MD
Email: Xiaqiong.Zhou@noaa.gov and henry.juang@noaa.gov

1. Introduction

The Global Forecast System (GFS) was updated from version 15 to 16 on 22 March, 2021. GFS.v16 has its number of vertical layers increased from 64 to 127 and model top extended from 54 km to 80 km. Physics parameterizations in GFS.v16 were also improved. It is the first major upgrade to the Finite-Volume Cubed-Sphere (FV3) dynamical core-based GFS (Lin and Rood, 1997; Putman and Lin, 2007) since its implementation for operation in 2019. Retrospective and real-time experiments were performed to evaluate the model performances. However, GFS.v16 encountered a few model instability failures from real-time parallel experiments. The diagnosis of these cases and the solutions proposed to remove the numerical instability are summarized in this study.

2. Diagnosis of failed cases

There were nine failed cases in total from the GFS.v16 real-time parallel experiment. The model integration was interrupted when the pressure thickness of a certain layer became negative or the thickness expressed in height became NaN (not-a-number). It was found that all these cases failed over a land grid when a strong tropical cyclone approached from the east. For example, the case initialized at 18Z UTC on 22 July 2020 failed when the eyewall of a strong tropical cyclone reached the Philippine east coast with strong onshore winds of about 40-50 m/s. By examining the model prognostic variables at each acoustic time step (12.5s), we found that the upward motion at lower levels at the grid points in question increased with time and then abruptly changed to unrealistically strong downdrafts (>300m/s) before the model crashed.

In the FV3 dynamic core for GFS.v16, the pressure perturbation p' and vertical velocity w tendency equations solved in a semi-implicit time-difference scheme are transformed to a tridiagonal matrix system of equations for w. This system requires coefficients and weights related to p' and layer thickness δz to solve w using the Thomas algorithm. In the corresponding subroutine for the non-hydrostatic adjustment, the layer-mean non-hydrostatic pressure perturbation is calculated first with $p' = p - p^*$, where p^* is hydrostatic pressure and p is full pressure, and can be calculated from the ideal gas law:

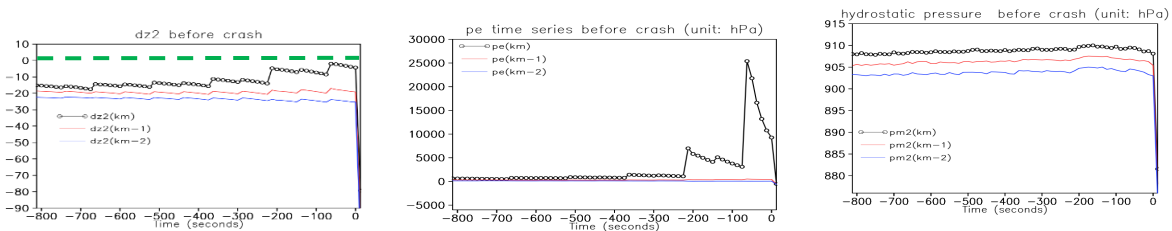$$p = \exp\left\{\gamma \log\left(-R_d \theta_v \frac{\partial m}{\partial z}\right)\right\} \qquad (1)$$

Figure 1. The time series of δz (left panel), full pressure (middle panel) and hydrostatic pressure (right panel) at the crash gridpoint. The black, red and blue curves represent the three lowest model levels km, km-1, km-2 respectively.

All the variables that are used to compute w are investigated. An unrealistic full pressure (>5000 hPa) is identified at the model lowest level at many acoustic steps (about 200 seconds) before the model crash, while the hydrostatic pressure and other variables remain to be normal (Fig. 1). The problem in the full pressure is further tracked back to the presence of an extreme small depth thickness at the lowest model layer where δz is very close to zero (Fig. 1). GFSv16 has 127 vertical layers with the lowest layer being about 20 m thick on average. It is unphysical for δz reaching to zero.

The forward-in-time advective processes are performed to generate the partially-updated geopotential height z before the non-hydrostatic adjustment in the FV3 dynamics. Note that the update of z through advection processes does not directly solve an equation for the volume of a grid cell, and it is forward-in-time as the sum of the advective height flux along the Lagrangian interfaces and the vertical distortion of the surfaces by the gradient of z. To solve z on the interfaces, the advecting winds are appropriately interpolated from layer means onto the layer interfaces by solving a tridiagonal system of equations based on the Parabolic Spline Method (PSM, Zerroukat et al. 2006) with high-order boundary conditions.

Figure 2 shows the time series of geopotential height at the break grid at the model lowest layers before and after the advection processes. The only evident change in terms of z with model integration is the increasing z at the model lowest level after advection, which is consistent with the decreasing of thickness depth seen in Figure 1.
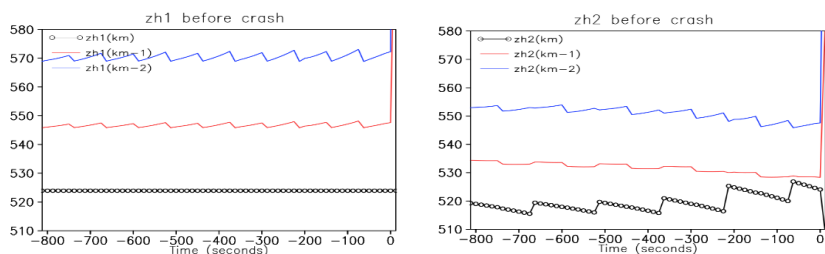

Figure 2. The time series of the geopotential height at the break grid at the model lowest three levels before (left panel) and after (right panel) the advection processes.

3. Potential solutions

An artificial limiter for the minimum thickness depth is defined in the FV3 dynamic code. This limiter is used with a value of 2 (meters) to enhance the monotonicity of height after the advection of z. We performed extensive sensitivity tests to stabilize the model with many other options and found that increasing the value of minimum thickness depth from 2 to 6 is the most effective and simple way to avoid model crashes. More importantly this fix has a very little impact on forecast skill. This temporary fix was implemented in GFSv16 to meet the model upgrade schedule.

Since the model instability issue likely originated from the advection of z at the model lowest level, we proposed to use zero-gradient boundary conditions (BCs), instead of high-order BCs, to reconstruct horizontal winds at the interfaces from layer means with PSM. The new BCs do not impact interior winds, except for smaller vertical gradients in the lowest model layers in the vertical. With the new BCs, all the originally failed cases were run successfully for 16 days in forecast length without applying the minimum thickness limiter.

The impact of this new method on model forecast was investigated in GFS.v16, the FV3-based limited area model and idealized mountain ridge experiments. Results show that this new method can effectively solve the model instability issues while incur little impact on forecast performance and the numerical solutions of idealized mountain waves.

References

Lin S.-J. and R. B. Rood, 1997: An explicit flux-form semi-Langrangian shallow-water model on the sphere, *Q. J. R. Meteorol. Soc.*, 123，2477-2498.
Putman, M. and S.-J. Lin, 2007: Finite-volume transport on various cubed-sphere grids. *J. Comp. Phys.*, 227, 55-78.
Zerroukat, M., Wood, N., and Staniforth, A. 2006: The Parabolic Spline Method (PSM) for conservative transport problems. *Inter. J. Num. Meth. in Flu.,* 51, 1297-1318.